Electronic Supplementary Information

$Co_{0.7}Fe_{0.3}$ NPs confined in yolk-shell N-doped carbon: engineering multi-beaded fibers as efficient bifunctional electrocatalyst for Zn-air battery

Ling Long,[a,b] Haohui Liu,[c] Jianbo Jia,[*,a,b,c] Yelong Zhang,[*,d] and Shaojun Dong [*,a,b]

[a] State Key Laboratory of Electroanalytical Chemistry, Changchun Institute of Applied Chemistry, Chinese Academy of Sciences, Changchun 130022, China

[b] University of Science and Technology of China, Hefei 230026, China

[c] School of Biotechnology and Health Sciences, Wuyi University, Jiangmen 529020, China

[d] School of Applied Physics and Materials, Wuyi University, Jiangmen 529020, P. R. China

*Corresponding author.

Email: jbjia@ciac.ac.cn or jbjiagu@163.com

Email: zhangyelong2008@126.com

Email: dongsj@ciac.ac.cn

Additional experimental section

1. Materials

Polyvinylpyrrolidone (PVP, k88-96) and cobalt chloride hexahydrate ($CoCl_2 \cdot 6H_2O$) were purchased from Aladdin. Iron(II) chloride tetrahydrate ($FeCl_2 \cdot 4H_2O$) and potassium hexacyanocobaltate(III) ($K_3[Co(CN)_6]$) were bought from MACKLIN. Polyacrylonitrile (PAN), Ruthenium(IV) oxide (RuO_2) and Nafion (5 wt%) were purchased from Sigma-Aldrich. Carbon-supported Pt catalyst (20 wt%, Pt/C) was bought form Johnson Matthey. N,N-dimethylformamide (DMF) was purchased from Tian in Fuyu Fine Chemical Co., Ltd. All chemicals were analytical grade and no further processing. All solutions were prepared with ultrapure water (resistivity: 18.25 MΩ cm).

2. Apparatus

The transmission electron microscopy (TEM) and high-resolution TEM (HRTEM) images were got with FEI TECNAI G^2, UK. The scanning electron microscopy (SEM) images were acquired from Philips XL30 ESEM FEG. X-ray diffraction (XRD) patterns were measured by a D8 Advance (Bruker, Germany, Cu Kα radiation, λ = 1.5406 Å) instrument. X-ray photoelectron spectroscopy (XPS) measurements were taken out on Esca Lab MKII X-ray photoelectron spectrometer (VG Scientific, UK). Inductively couple plasma-optical emission spectrometer (ICP-OES) was measured on a PerkinElmer ICP instrument. The three-electrode system was used to carry on all of the electrochemical measurements, namely the catalyst modified glassy carbon electrode (GCE) as the working electrode, saturated Ag/AgCl as the reference electrode and graphite rod as the counter electrode. The electrochemical impedance spectroscopy (EIS) was performed on CHI660E electrochemical workstation. The rotating ring-disk electrode (RRDE) techniques and cyclic voltammetry (CVs) were conducted on CHI842B electrochemical workstation. The measured potential (against an Ag/AgCl reference electrode) was converted to a reversible hydrogen electrode (RHE) according to RHE calibration: E(vs. RHE) = E(vs. Ag/AgCl) + 0.059pH + 0.197.

3. Electrocatalytic activity evaluation

First, 2 mg mL^{-1} of catalyst was uniformly dispersed into solution (water, isopropanol and Nafion with a volume ratio of 21:21:0.15) by ultrasound. Then, the ink was dropped onto the GCE surface with the loading amount of 1.0 and 0.429 mg cm^{-2} for ORR and OER tests, respectively. For comparison, the commercial Pt/C and RuO_2 were modified onto the electrode surface with the loading mass of 25 μg_{Pt} cm^{-2} and 0.429 mg_{RuO2} cm^{-2}, respectively. The surface area of the glassy carbon electrode is 0.07 cm^2, and the surface areas of the ring and disk electrodes on the rotating ring-disk electrode (RRDE) are 0.188 and 0.126 cm^2, respectively.

The linear sweep voltammetry (LSV) curves for OER experiments were performed in a 1.0 M KOH solution with a potential range of 1.023 ~ 1.623 (vs. RHE) and a scan rate of 5 mV s^{-1}. The ORR experiments were performed in O_2-saturated 0.10 M KOH solution. The RRDE curves were acquired at the potential range from 1.162 ~ 0.162 V (vs. RHE) with a rotating speed of 1600 rpm and a scan rate of 5 mV s^{-1}. A background subtraction of RRDE curves for all prepared catalysts was performed (deducting the RRDE tested in a saturated N_2 solution). The ring potential was set 1.162 V in 0.10 M KOH. Before both OER and ORR experiments, all the modified electrodes were activated in the corresponding potential range and electrolyte by 40 CV cycles with a sweep rate of 50 mV s^{-1}. The EIS was tested in a 1.0 M KOH solution at

0.52 V (vs. RHE) with a frequency range from 0.1 to 100000 HZ, and amplitude of 5 mV. The calculation formula of H_2O_2 yield (H_2O_2%) and electron transfer number (n) is as follows:

$$H_2O_2\% = \frac{200\frac{I_r}{N}}{I_d + \frac{I_r}{N}}$$

$$n = \frac{4I_d}{I_d + \frac{I_r}{N}}$$

Wherein, N is the current collection efficiency (calculated as 0.44), I_d and I_r are the disk current and ring current, respectively.

ORR LSV curves at various rotating speeds were recorded to calculate the n during the ORR process based on the Koutecky-Levich equation:

$$\frac{1}{J} = \frac{1}{J_L} + \frac{1}{J_K} = \frac{1}{B\omega^{1/2}} + \frac{1}{J_K}$$

$$B = 0.62nFC_0(D_0)^{2/3}V^{-1/6}$$

Where J is the measured current density, J_K and J_L are the kinetic and limiting current densities, ω is the angular velocity of the rotating disk. n is the electron transfer number, F is the Faraday constant (96485 C mol^{-1}), C_0 is the bulk concentration of O_2 in 0.10 M KOH solution (1.2×10^{-6} mol cm^{-3}), D_0 is the diffusion coefficient of O_2 (1.9×10^{-5} cm^2 s^{-1}), and *V* is the kinematic viscosity of 0.10 M KOH solution (0.01 cm^2 s^{-1}).

4. Zn-air batteries assembly

The used air cathode was first made by dropping a certain amount of catalyst inks onto the surface of the carbon paper substrate at room temperature, and then dried overnight in a vacuum oven at 60 °C. A homemade Zn-air battery was fabricated with a $Co_{0.7}Fe_{0.3}$@$NC_{2:1}$-*800*-based cathode, a Zn foil anode, and an aqueous alkaline electrolyte (7 M KOH + 0.2 M $ZnCl_2$). Both the specific capacity and energy density values were calculated based on the mass of consumed Zn during the discharge process. For comparison purposes, the commercial catalysts (20 wt% Pt/C: RuO_2 = 1:1, mass ratio) structured battery were also tested. The loading was 0.1 mg cm^{-2} for all materials. The electrochemical characterizations of the batteries were performed with a Land CT2001A battery test system.

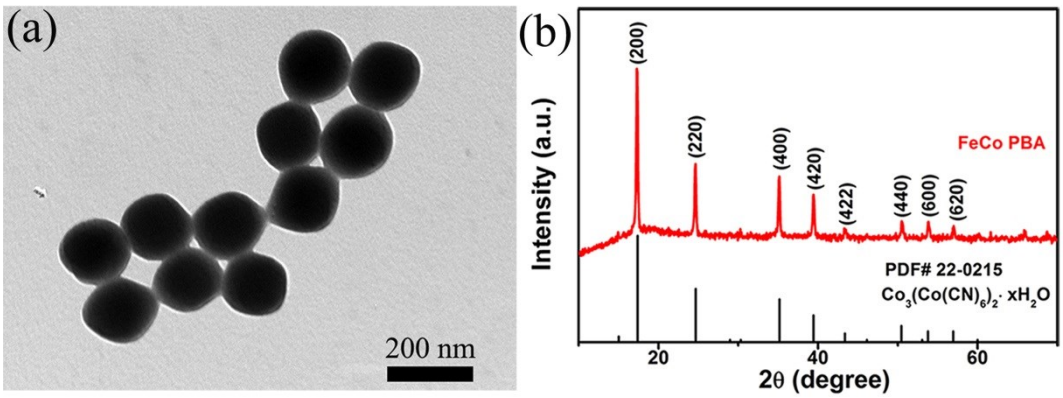

Fig. S1 (a) TEM image and (b) XRD pattern of FeCo PBA. The prepared FeCo PBA is uniformly distributed solid nanospheres with average size of ~160 nm. XRD pattern shows all the characteristic diffraction peaks are in good agreement with $Co_3[Co_9(CN)_6]_2 \cdot xH_2O$ (PDF#22-0215), demonstrating the high purity of the synthesized FeCo PBA sample.

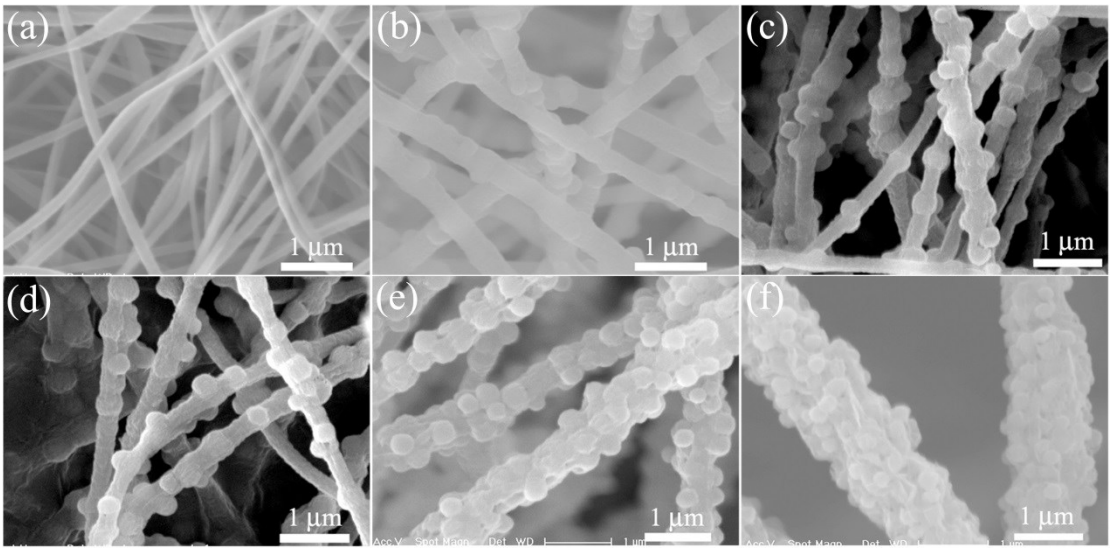

Fig. S2 SEM images of (a) Pure PAN fibers, (b-f) FeCo PBA@PAN$_{X:Y}$ electrospinning under different precursor ratios (PBA : PAN). (b) 1:2, (c) 2:3, (d) 1:1, (e) 2:1, (f) 3:1.

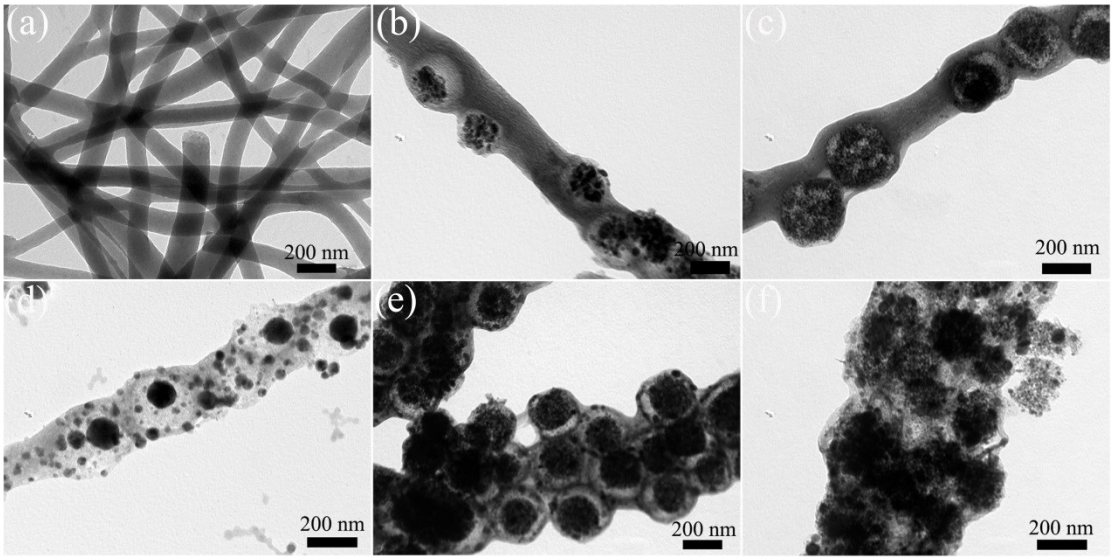

Fig. S3 TEM images of (a) NC fibers, (b) $Co_{0.7}Fe_{0.3}$@$NC_{1:2}$-*800*, (c) $Co_{0.7}Fe_{0.3}$@$NC_{2:3}$-*800*, (d) $Co_{0.7}Fe_{0.3}$@$NC_{1:1}$-*800*, (e) $Co_{0.7}Fe_{0.3}$@$NC_{2:1}$-*800*, (f) $Co_{0.7}Fe_{0.3}$@$NC_{3:1}$-*800*.

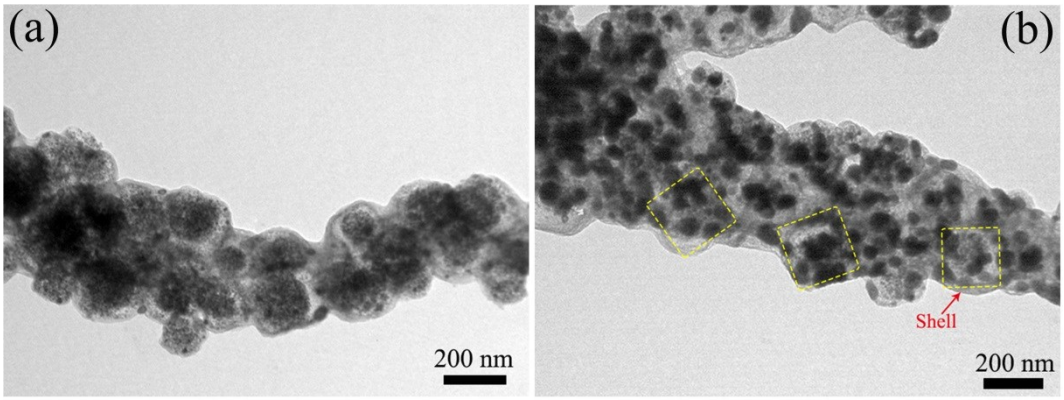

Fig. S4 TEM images of (a) $Co_{0.7}Fe_{0.3}$@$NC_{2:1}$-*700* and (b) $Co_{0.7}Fe_{0.3}$@$NC_{2:1}$-*900*.

The influence of the template and calcination temperature on the morphology.

In order to investigate the influence of the template on the $Co_{0.7}Fe_{0.3}$@NC electrocatalyst, we fabricated a series of electrospun membranes with different FeCo PBA/PAN mass ratios, which named as FeCo PBA@$PAN_{X:Y}$. From Fig. S2 we can observe that the surface of pure PAN fibers are smooth. After incorporated with FeCo PBA, the diameter of fiber increases significantly and all FeCo PBA nanospheres are threaded along the one-dimensional fibers. The microstructure of electrospinning fibers is modulated by the FeCo PBA/PAN mass ratio. As the mass ratio varied from 1:2 to 3:1, the diameter of fibers and the density of nanospheres continue to increase, the morphology of each fiber transformed from a necklace-like

(1:2 ~ 1:1) to a multiple bead-like (2:1, 3:1). Fibers with different morphology can be tuned by changing the amount of templates in spinning solution, which is based on the difference viscosity of spinning solution.

The similar morphological changes can also see from Fig. S3. After heat treatments of FeCo PBA@PAN$_{X:Y}$, a necklace-like or multi-bead-like morphology constructed by yolk-shell or solid active units was obtained. The average size of each nano-unit is similar to FeCo PBA, which proves that the solid FeCo PBA nanospheres were successfully spun into the fibers. When excessive FeCo PBA nanospheres are embedded, the electrospun fibers become too thick. In that case, most of FeCo PBA is tightly wrapped in the fiber and the internal FeCo PBA can hardly be decomposed and shrunk to form yolk-shell structure at short calcination time. The properties of the yolk-shell will be disappeared, and only the solid nanospheres can be seen wrapped in the fibers (Fig. S3(f)).

In addition, Fig. S4 reveals the effect of calcination temperature on the catalyst morphology. The multi-bead structure composed of yolk-shell nano-units is still preserved under different temperatures. However, increasing the temperature to 900 °C will cause a large number of aggregated large particles. The internal core is not obvious, but the outer shell can still be observed (Fig. S4(b)).

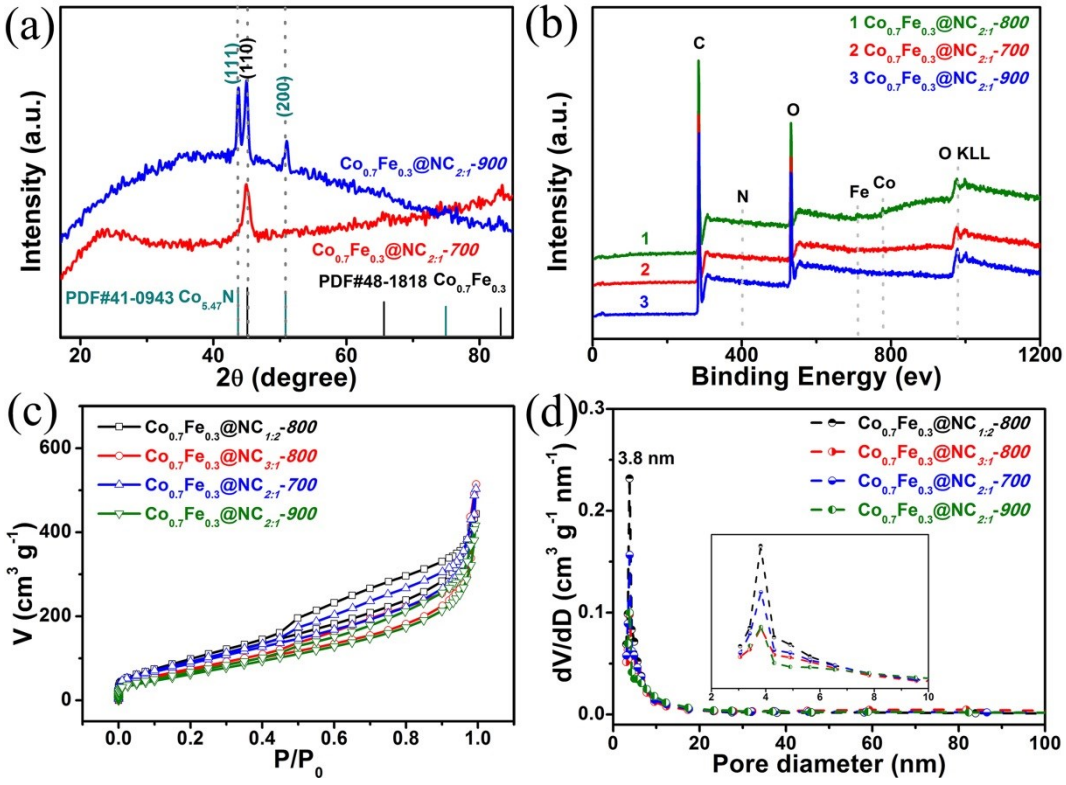

Fig. S5 (a) XRD patterns and (b) XPS spectra of $Co_{0.7}Fe_{0.3}$@NC$_{X:Y}$-*T*. (c) Nitrogen adsorption-desorption isotherm curve and (d) BJH pore size distribution of the $Co_{0.7}Fe_{0.3}$@NC$_{X:Y}$-*T*.

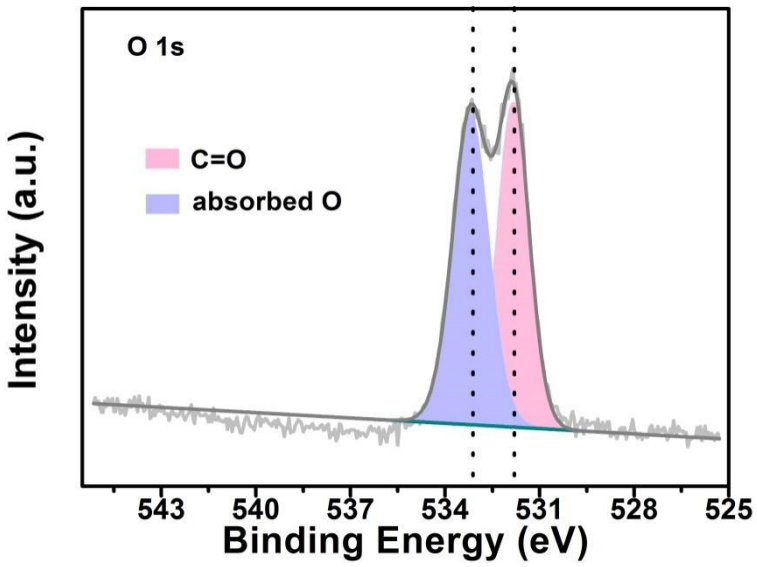

Fig. S6 High-resolution XPS spectrum of O 1s in $Co_{0.7}Fe_{0.3}@NC_{2:1}$-*800*.

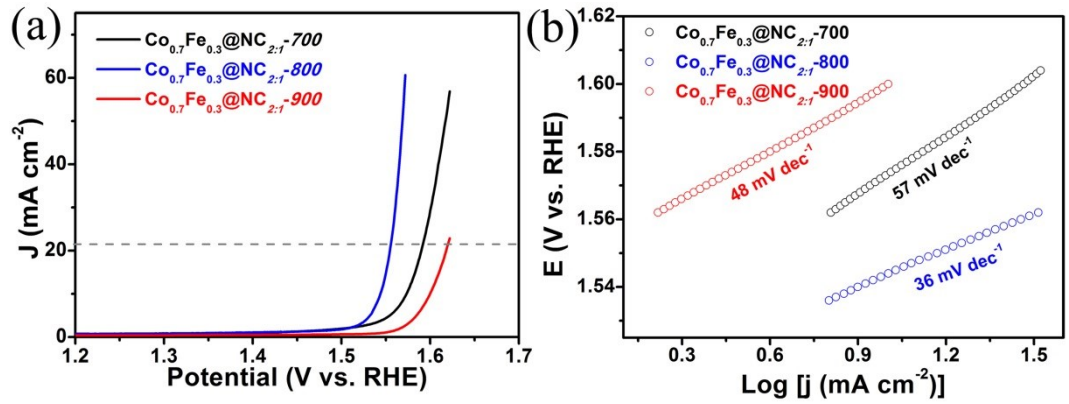

Fig. S7 (a) LSV curves and (b) corresponding Tafel slopes of $Co_{0.7}Fe_{0.3}@NC_{2:1}$-*T* (*T* = 700, 800, 900 °C) for OER in 1.0 M KOH at 5 mV s^{-1}.

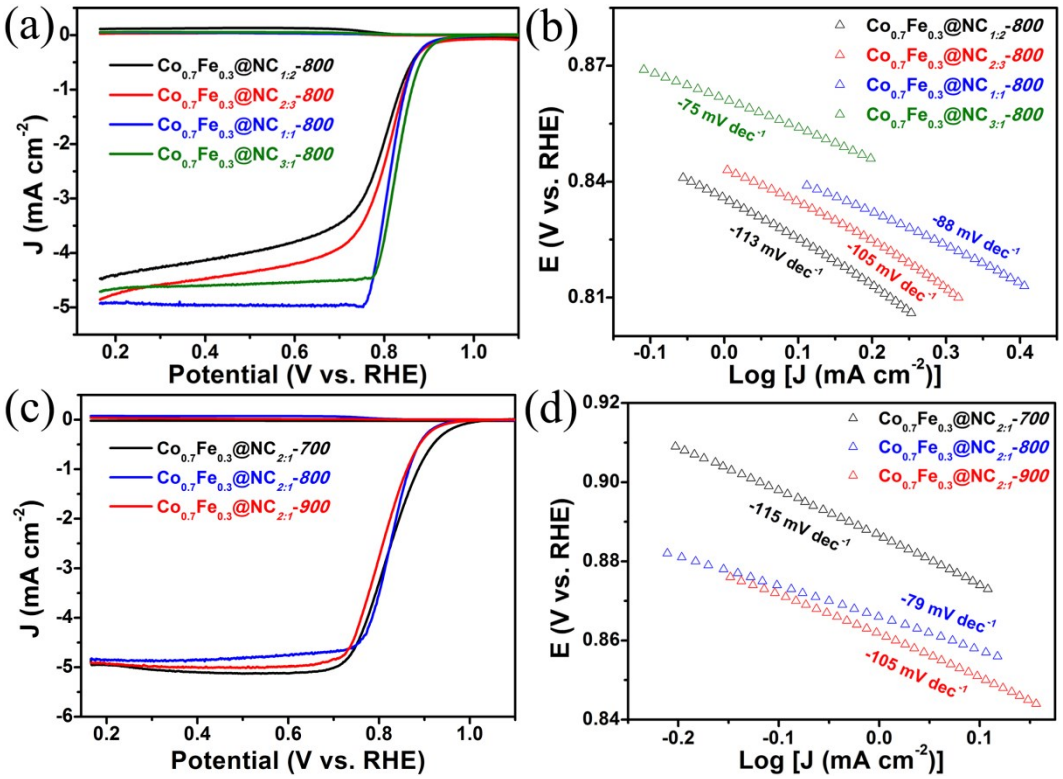

Fig. S8 (a) RRDE voltammograms and (b) Tafel slopes of $Co_{0.7}Fe_{0.3}@NC_{X:Y}$-*800*, (c) RRDE voltammograms and (d) Tafel slopes of $Co_{0.7}Fe_{0.3}@NC_{2:1}$-*T* in O_2-saturated 0.10 M KOH solution. The scan rate is 5 mV s^{-1} and the rotation rate is 1600 rpm.

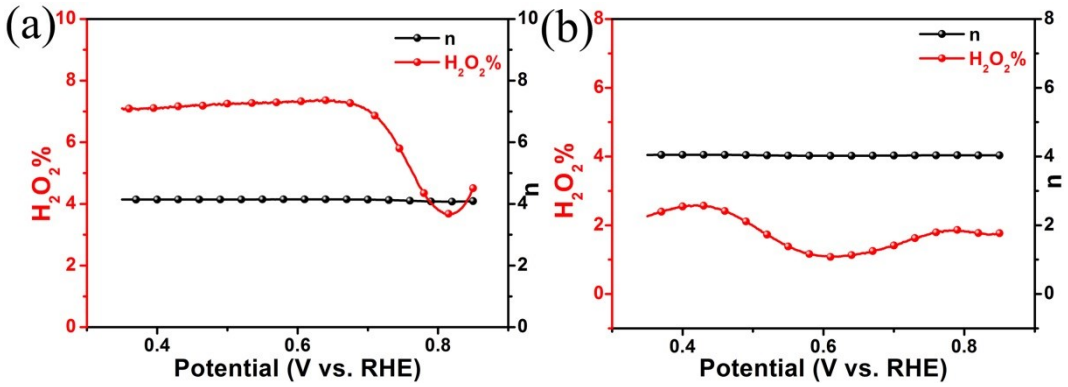

Fig. S9 H_2O_2% and electron transfer number (n) of (d) $Co_{0.7}Fe_{0.3}@NC_{2:1}$-*800* and (b) commercial Pt/C in O_2-saturated 0.10 M KOH solution.

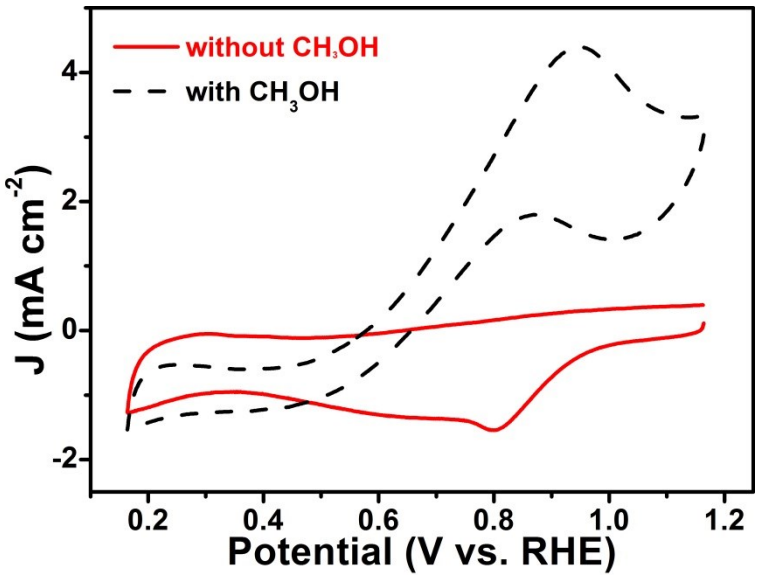

Fig. S10 CVs of the commercial Pt/C in O_2-saturated 0.10 M KOH without and with 1.0 M CH_3OH at a scan rate of 50 mV s^{-1}.

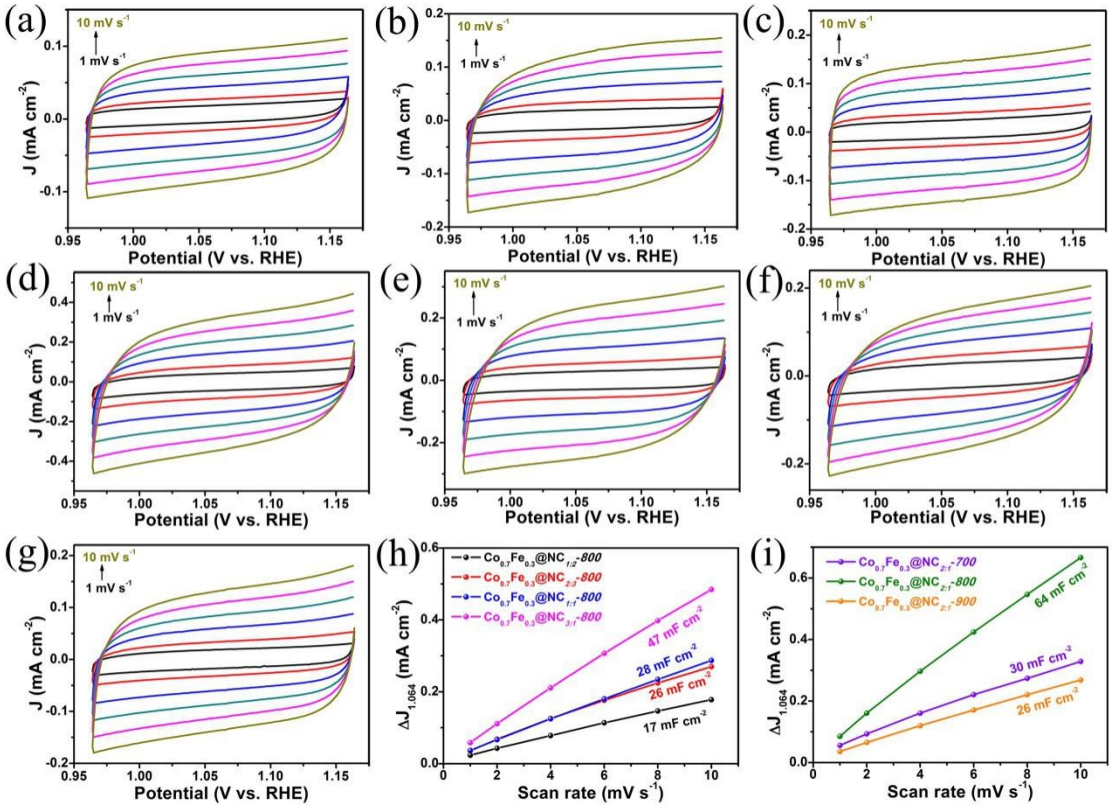

Fig. S11 CVs of (a) $Co_{0.7}Fe_{0.3}@NC_{1:2}$-*800*, (b) $Co_{0.7}Fe_{0.3}@NC_{2:3}$-*800*, (c) $Co_{0.7}Fe_{0.3}@NC_{1:1}$-*800*, (d) $Co_{0.7}Fe_{0.3}@NC_{2:1}$-*800*, (e) $Co_{0.7}Fe_{0.3}@NC_{3:1}$-*800*, (f) $Co_{0.7}Fe_{0.3}@NC_{2:1}$-*700*, (g) $Co_{0.7}Fe_{0.3}@NC_{2:1}$-*900* in 0.10 M KOH at different scan rates (1, 2, 4, 6, 8, and 10 mV s^{-1}). (h, i) Plots of ΔJ vs. scan rate at 1.064 V for $Co_{0.7}Fe_{0.3}@NC_{X:Y}$-*T* in 0.10 M KOH.

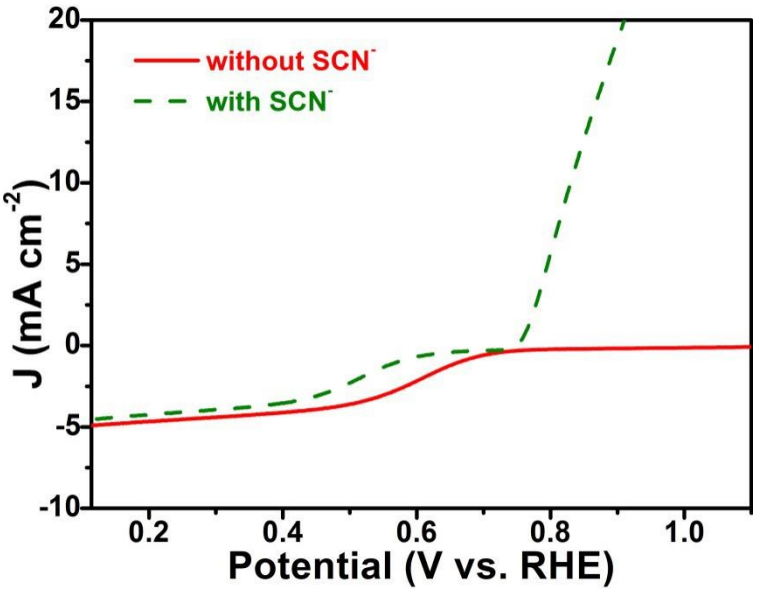

Fig. S12 ORR LSV curves of $Co_{0.7}Fe_{0.3}@NC_{2:1}$-*800* in O_2-saturated 0.50 M H_2SO_4 with and without 10 mM SCN^-.

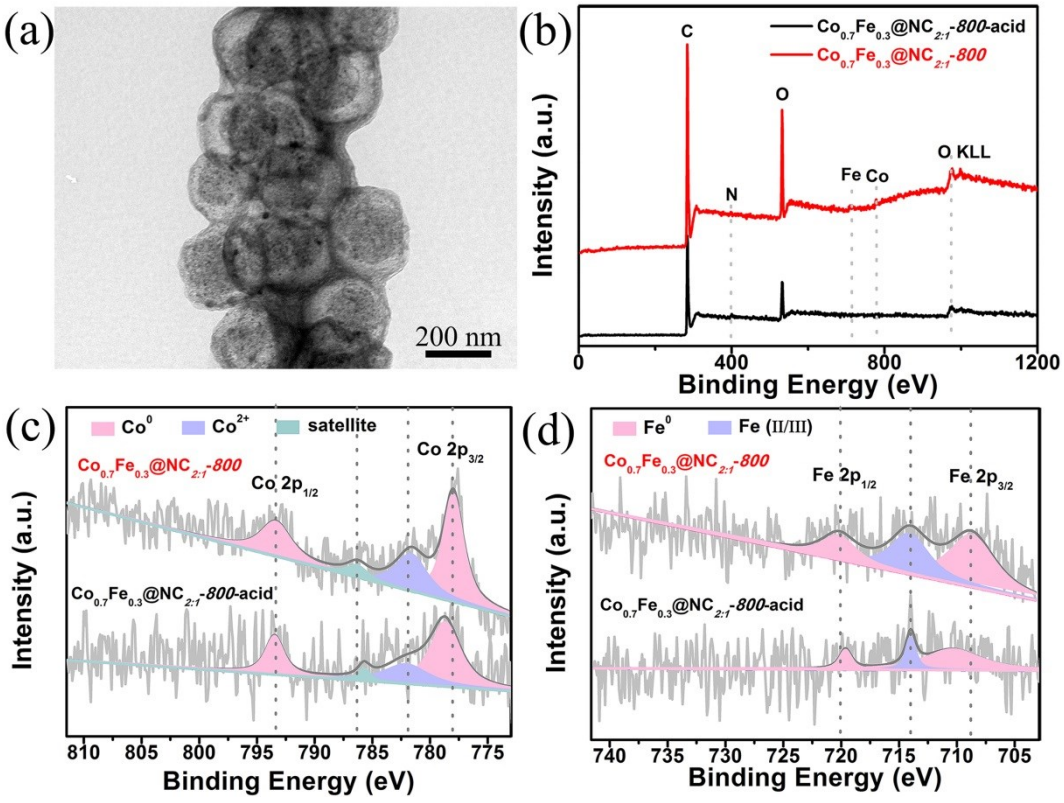

Fig. S13 (a) TEM image and (b-d) XPS spectra of $Co_{0.7}Fe_{0.3}@NC_{2:1}$-*800*-acid.

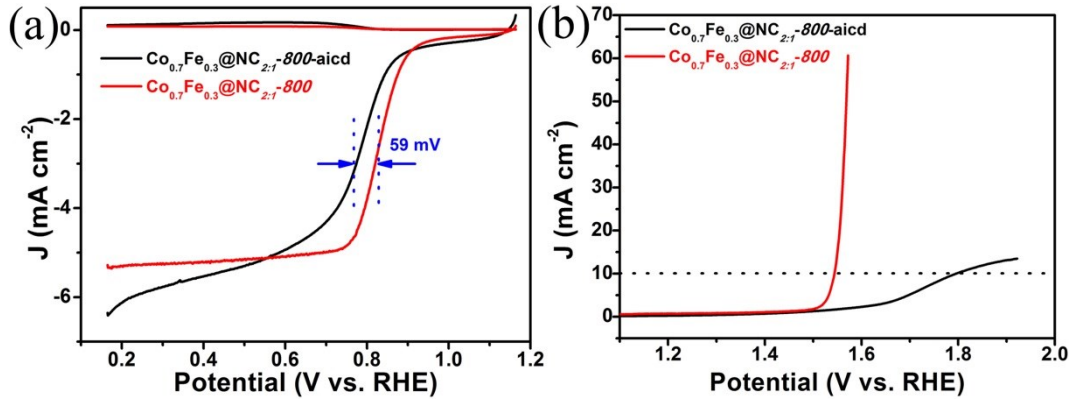

Fig. S14 (a) RRDE voltammograms for ORR and (b) LSV curves for OER of $Co_{0.7}Fe_{0.3}@NC_{2:1}$-*800* and $Co_{0.7}Fe_{0.3}@NC_{2:1}$-*800*-acid. RRDE curves in (a) do not perform background correction.

Fig. S15 Photograph of the Zn-air battery employing the commercial cathode, giving an open-circuit potential of 1.394 V.

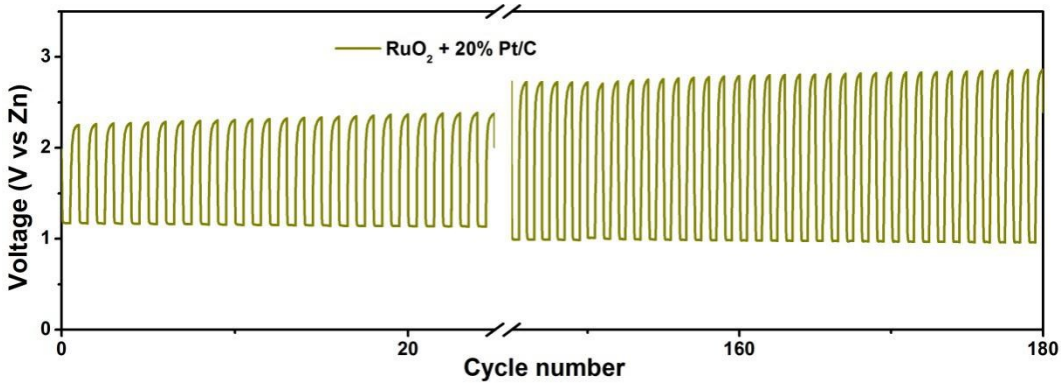

Fig. S16 Charge/discharge curves of the Zn-air battery with a commercial cathode at a current density of 10 mA cm^{-2} (20 min per cycle).

Table S1 The BET surface area, pore diameter and XPS elemental analyses in different $Co_{0.7}Fe_{0.3}@NC_{X:Y}$-*T*.

Catalyst	BET surface area (m^2 g^{-1})	Pore diameter (nm)	C (at.%)	O (at.%)	Fe (at.%)	Co (at.%)	N (at.%)
$Co_{0.7}Fe_{0.3}@NC_{1:2}$-*800*	346.1	3.8	87.4%	11.51%	0.23%	0.39%	0.46%
$Co_{0.7}Fe_{0.3}@NC_{2:1}$-*800*	**743.8**	**3.8**	**81.45%**	**17.04%**	**0.21%**	**0.45%**	**0.86%**
$Co_{0.7}Fe_{0.3}@NC_{3:1}$-*800*	274.7	3.8	89.18%	10.24%	0.18%	0.22%	0.18%
$Co_{0.7}Fe_{0.3}@NC_{2:1}$-*700*	351.4	3.8	69%	19.78%	0%	0.1%	0.43%
$Co_{0.7}Fe_{0.3}@NC_{2:1}$-*900*	255.6	3.8	83.1%	16.54%	0%	0.08%	0.27%

Table S2 Comparison of OER performance of $Co_{0.7}Fe_{0.3}@NC_{2:1}$-*800* with recently reported analogous Fe/Co-based electrocatalysts.

Catalyst	Electrolyte	Overpotential (at 10 mA cm^{-2})	Refs.
S, N codoped carbon cubes embedding Co-Fe carbides	1.0 M KOH	330 mV	[1]
Cobalt nanoparticles embedded N-doped carbon hollow nanocages	1.0 M KOH	350 mV	[2]
Hollow FeCo alloy nanoparticles assembled in the N-doped carbon nanofibers	1.0 M KOH	368 mV	[3]
N-doped carbon nanotube supported ultrathin N-doped carbon coated $Fe_{1.2}Co$ nanoparticles	0.10 M KOH	355 mV	[4]
Nitrogen-doped carbon nanofibers encapsulated FeCo alloy nanoparticles-800	0.10 M KOH	456 mV	[5]
FeCo/N-doped "dual-network" carbon aerogels	0.10 M KOH	390 mV	[6]
FeCo-N/C	0.10 M KOH	370 mV	[7]
FeCo bimetallic alloy nanoparticles anchored on biomass-processed porous N-carbon	0.10 M KOH	380 mV	[8]
N, O-codoped graphene nanorings-integrated boxes-800	1.0 M KOH	400 mV	[9]
FeCo alloy nanoparticles embedded in the N-doped carbon nanotubes-grafted N and S co-doped carbon nanofibers	0.1 M KOH	360 mV	[10]
$Co_{0.7}Fe_{0.3}@NC_{2:1}$-*800*	**1.0 M KOH**	**314 mV**	**This work**

Table S3 R_{ct} and C_{dl} of $Co_{0.7}Fe_{0.3}@NC_{X:Y}$-*T* catalyst.

Catalyst	R_{ct} (Ω)	C_{dl} (mF cm^{-2})
$Co_{0.7}Fe_{0.3}@NC_{1:2}$-*800*	128.1	17
$Co_{0.7}Fe_{0.3}@NC_{2:3}$-*800*	103.9	26
$Co_{0.7}Fe_{0.3}@NC_{1:1}$-*800*	81.04	28
$Co_{0.7}Fe_{0.3}@NC_{2:1}$-*800*	**54.54**	**64**
$Co_{0.7}Fe_{0.3}@NC_{3:1}$-*800*	113.3	47
$Co_{0.7}Fe_{0.3}@NC_{2:1}$-*700*	100.7	30
$Co_{0.7}Fe_{0.3}@NC_{2:1}$-*900*	158.9	26

Table S4. Comparison of the ORR activity of $Co_{0.7}Fe_{0.3}@NC_{X:Y}$-*T* and Pt/C.

	$Co_{0.7}Fe_{0.3}@NC_{X:Y}$-*800*					**$Co_{0.7}Fe_{0.3}@NC_{2:1}$-*T***		**Pt/C**
	1:2	2:3	1:1	**2:1**	3:1	700	900	
E_{onset} (V)	0.925	0.937	0.923	**0.958**	0.945	0.982	0.952	0.964
$E_{1/2}$ (V)	0.792	0.799	0.814	**0.827**	0.832	0.824	0.811	0.818
Tafel slope (mV dec^{-1})	-113	-105	-88	**-79**	-75	-115	-105	-109

The potential value corresponding to the current density of 0.1 mA cm^{-2} selects as the E_{onset}.

Table S5. Comparison of the ORR activity of $Co_{0.7}Fe_{0.3}@NC_{2:1}$-*800* with recently reported analogous Fe/Co-based catalysts O_2 saturated-0.1 M KOH.

Catalyst	$E_{1/2}$ (V)	E_{onset} (V)	Refs.
Cobalt nanoparticles embedded N-doped carbon hollow nanocages	0.77	0.88	[2]
N-doped carbon nanotube supported ultrathin N-doped carbon coated $Fe_{1.2}Co$ nanoparticles	0.82	0.842	[4]
N-doped carbon nanofibers encapsulated FeCo alloy nanoparticles-800	0.817	0.907	[5]
FeCo/N-doped "dual-network" carbon aerogels	0.81	0.89	[6]
FeCo-N/C	0.84	0.98	[7]
N, O-codoped graphene nanorings-integrated boxes-800	0.84	0.92	[9]
FeCo/N-doped porous carbon nanosheets	0.81	0.92	[11]
Sugarcane-derived FeCo-N@N-doped carbon	0.81	0.91	[12]
FeCo@NCs-0.15	0.83	/	[13]
$Co_{0.7}Fe_{0.3}@NC_{2:1}$-*800*	**0.827**	**0.958**	**This work**

Table S6 Comparison of the performance of rechargeable liquid Zn-air batteries between our work and other reported alloy-based carbon eletrocatalysts.

Samples	Peak power density (mW cm^{-2})	Specific capacity (mAh g_{Zn}^{-1})	Energy density (Wh kg_{Zn}^{-1})	Initial charge/ discharge voltage gap (V)	Durability (h)	Ref.
$Co_{0.7}Fe_{0.3}$@$NC_{2:1}$-*800*	**85.7**	**622.5**	**712.3**	**0.835**	**20 min/cycle for 180 cycles, voltage gap increased ~0.32 V**	**This work**
RuO_2 + 20 wt.% Pt/C	**63.8**	**585.7**	**627.4**	**1.077**	**20 min/cycle for 180 cycles, voltage gap increased ~0.81 V**	**This work**
N-GCNT/FeCo-3[a]	89.3	872.2	653.2	0.26	10 min/cycle for 240 cycles	14
Ni_3Fe/Co-N-C[b]	68	/	/	0.75	discharge/charge cycles for 65 h, increased ~0.21 V	15
FeCo-NCNFs-800[c]	74	/	/	0.88	2500 min, voltage gap increased ~0.11 V	5
FeCo@C MS[d]	86.09	503	639	0.71	10 min/cycle for 373 cycles, voltage gap increased ~0.58 V	16
$Fe_{0.5}Ni_{0.5}$@N-GR[e]	85	765	940	0.8	40 h	17
Ni_3Fe/N-C[f]	/	528	634	/	105 cycles for 420 h	18

a: bimetal FeCo nanoparticles enveloped by N-doped graphitic carbon nanotubes

b: homogeneously disperse Ni_3Fe nanoparticle on Co-N-C.

c: nitrogen-doped carbon nanofibers encapsulated FeCo alloy nanoparticles

d: dual-phase FeCo-based nanoparticles@heteroatomdoped carbon microspheres

e: $Ni_{0.5}Fe_{0.5}$@N-graphite

f: Ni_3Fe nanoparticles embedded in porous nitrogen-doped carbon sheets

References

1 Y. B. Lian, K. F. Shi, H. J. Yang, H. Sun, P. W. Qi, J. Ye, W. B. Wu, Z. Deng and Y. Peng, *Small*, 2020, **16**, 1907368.

2 Y.-N. Hou, Z. Zhao, H. Zhang, C. Zhao, X. Liu, Y. Tang, Z. Gao, X. Wang and J. Qiu, *Carbon*, 2019, **144**, 492-499.

3 Y. Y. Ma, W. J. Zang, A. Sumboja, L. Mao, X. M. Liu, M. Y. Tan, S. J. Pennycook, Z. K. Kou, Z. L. Liu, X. Li and J. Wang, *Sustain. Energ. Fuels*, 2020, **4**, 1747-1753.

4 S. S. Li, W. H. Chen, H. Z. Pan, Y. W. Cao, Z. Q. Jiang, X. N. Tian, X. G. Hao, T. Maiyalagan and Z. J.

Jiang, *ACS Sustain. Chem. Eng.*, 2019, **7**, 8530-8541.

5 L. Yang, S. Feng, G. Xu, B. Wei and L. Zhang, *ACS Sustain. Chem. Eng.*, 2019, **7**, 5462-5475.

6 G. T. Fu, Y. Liu, Y. F. Chen, Y. W. Tang, J. B. Goodenough and J. M. Lee, *Nanoscale*, 2018, **10**, 19937-19944.

7 H. X. Shui, T. Jin, J. Hu and H. L. Liu, *ChemElectroChem*, 2018, **5**, 1401-1406.

8 J. J. Liu, T. He, Q. C. Wang, Z. X. Zhou, Y. Q. Zhang, H. Q. Wu, Q. Li, J. Zheng, Z. F. Sun, Y. P. Lei, J. M. Ma and Y. Zhang, *J. Mater. Chem. A*, 2019, **7**, 12451-12456.

9 Q. Hu, G. M. Li, G. D. Li, X. F. Liu, B. Zhu, X. Y. Chai, Q. L. Zhang, J. Liu and C. He, *Adv. Energy Mater.*, 2019, **9**, 1803867.

10 K. Fu, Y. Wang, L. C. Mao, X. X. Yang, W. Peng, J. H. Jin, S. L. Yang and G. Li, *J. Power Sources*, 2019, **421**, 68-75.

11 R. Gao, Y. Yin, F. Niu, A. Wang, S. Li, H. Dong and S. Yang, *ChemElectroChem*, 2019, **6**, 1824-1830.

12 H. C. Kuo, S. H. Liu, Y. G. Lin, C. L. Chiang and D. C. W. Tsang, *Catal. Sci. Technol.*, 2020, **10**, 3949-3958.

13 X. Luo, H. Ren, H. Ma, C. Yin, Y. Wang, X. Li, Z. Shen, Y. Wang and L. Cui, *J. Colloid Interf. Sci.*, 2020, **569**, 267-276.

14 C.-Y. Su, H. Cheng, W. Li, Z.-Q. Liu, N. Li, Z. Hou, F.-Q. Bai, H.-X. Zhang and T.-Y. Ma, *Adv. Energy Mater.*, 2017, **7**, 1602420.

15 J. B. Tan, T. Thomas, J. X. Liu, L. Yang, L. H. Pan, R. Cao, H. J. Shen, J. C. Wang, J. Liu and M. H. Yang, *Chem. Eng. J.*, 2020, **395**, 125151.

16 Y. T. Xu, B. L. Chen, J. Nie and G. P. Ma, *Nanoscale*, 2018, **10**, 17021-17029.

17 P. T. Liu, D. Q. Gao, W. Xiao, L. Ma, K. Sun, P. X. Xi, D. S. Xue and J. Wang, *Adv. Funct. Mater.*, 2018, **28**, 1706928.

18 G. Fu, Z. Cui, Y. Chen, Y. Li, Y. Tang and J. B. Goodenough, *Adv. Energy Mater.*, 2017, **7**, 1601172.